Egyptian Journal of Chemistry

http://ejchem.journals.ekb.eg/

Nonlinear Regression of Rare Earth Metal Ions [Y^{3+} and La^{3+}] Adsorption Upon Multifunctionalized Poly(glycidylmethacrylate)

Nilly A. Kawady [a]*, Ebrahium AbdelGwad [a], Sally S. Muhammad [a]*, Reda M. Attia [a], Randa Salah Eldin Mohamed [a], Said E. Mohammady [a], Ahmad A. Tolba [a], Marwa M. Rashad [a], Zeinab M. Shalaby [a], Ahmed A. Galhoum [a]*

[a] *Nuclear Materials Authority, P.O. Box 530, El-Maadi, Cairo, Egypt*

Abstract

The recovery of two rare earth metal ions (REs) [Y^{3+} and La^{3+}, belonging to heavy and light REs, respectively] was studied using functionalized poly(glycidylmethacrylate) adsorbent (F-PGMA) modified with polyaminophosphonic acid moieties. By using CHNP/O, BET, SEM, pH-titration, XRD, XPS, and FTIR analysis techniques, the structure of the synthesized adsorbent was clarified. The adsorption properties toward Y^{3+} and La^{3+} were compared and the interaction behaviors were explained with XPS and FTIR analysis. The saturation adsorption capacities (in mmol.g^{-1}) have the following order: La^{3+} (0.795) > Y^{3+} (0.744) at optimal pH_0 5.0. The adsorption was endothermic with fast kinetics (180/240 min) and the adsorption half-time ($t_{1/2}$) 16.2 and 29.3 min for La^{3+} and Y^{3+}, respectively. Langmuir and pseudo-second-order equations (PSO) fit well experimental data. Also, the possible complexes structures were explained. According to the adsorption test in bi-system solution, $K_{SC}(La^{3+}/Y^{3+})$ was about 1.7. Desorption and adsorbent recycling were successfully achieved using HNO_3 solution (0.5 M). The F-PGMA shows high durability over six cycles with desorption efficiency >93% and >95% for La^{3+} and Y^{3+}, respectively. The adsorption process was described quantitatively using novel three-dimensional (3D) nonlinear mathematical model. The advanced theoretical studies were achieved by the MATLAB software, utilizing a variety of models. The data were then fitted using a successive approximations approach with many trails. The Floatotherm included Van't Hoff parameters model was revels the endothermic and spontaneous behaviors of the adsorption process. Vermeulen model of the binary system indicates that, the adsorption process was achieved with a synergism behavior and the Y element exhibited more competition than La.

Keywords: Poly(glycidylmethacrylate), Multifunctionalization, Polyaminophosphonic groups, Lanthanum and yttrium, Nonlinear modeling, Vermeulen binary system model

1. Introduction

Due to science and technology progression, the capability of rare earth elements (REs) which called "industrial gold" has been actively investigated in a variety of disciplines, and some REs are thought to be extremely beneficial additives in the high-tech industry and various fields (e.g., nuclear energy, photovoltaic, metallurgical industries, etc.) [1-5]. Many of the electronic gadgets we use on a daily basis and a wide range of industrial applications, including as automotive, electronics, aerospace, clean energy, and defense, all depend on REs. Because of their catalytic and luminous qualities, REs are also commonly used in high-tech and "green" products [6, 7]. REs are a group of 17 strongly related heavy elements that comprise scandium, yttrium and the lanthanide group [2, 6]. Consequently, the separation and recovery of rare earths from industrial and mining wastewater is crucial for economic and technological reasons and also for the potential environmental threats [6, 7]. To date, numerous technological solutions have been utilized to cope with industrial wastes [1, 8].

More specifically, due to its high effectiveness and ease of operation on a wide scale, adsorption has

*Corresponding author e-mail: Nilly A. Kawady (nillykawady@yahoo.com), Sally S. Muhammad (sally_rose79@hotmail.com) , Ahmed A. Galhoum (Galhoum_nma@yahoo.com) .

Receive Date: 29 January 2023, **Revise Date:** 27 February 2023, **Accept Date:** 05 March 2023,
First Publish Date: 05 March 2023
DOI: 10.21608/EJCHEM.2023.189494.7529

been proven to be one of the most successful methods for extracting and recovering REs^{3+} from wastewaters. [5-7, 9, 10]. Herein, the extremely reactive monomer glycidylmethacrylate (GMA), which has vinyl and epoxy functionalities, satisfies the criteria for post-polymerization and chemical-modification [3, 4, 11]. Generally, the anchored and attached molecules have N–, O–, S– or P–atoms, or a mixture of these elements, can serve as basic centers for complexing cations and enabling selective separation [10-12]. By similarity with synthetic polymers/resins [11, 13], organophosphorus derivatives are recognized as effective metal complexing agents [14] and used as industrial chemicals in metal extraction [9], water treatment [11], and pollution control [4, 13]. Recently, computer technology development has made it easier to apply the nonlinear regression optimization method as a substitute for determining isothermal, kinetic, and thermodynamics parameter values [15, 16]. Therefore, simulation suitable techniques for its representation and processing must be developed in order to handle data effectively. The importance of kinetics utilization for the chemical describes the mechanism and rate of adsorption of REs^{3+} (e.g., La^{3+} and Y^{3+}) upon a specific adsorbent. Vermeulen model present an explicit multicomponent adsorption model for components; like binary or ternary system, which obeying whether Langmuir or/and any other isotherm in a mono system adsorption case. Consequently, e.g. Langmuir isotherm can be expanded using Taylor expansion series and correlated to produce the modified Vermeulen model [15, 17]. The purpose of this work is synthesis and utilizing a micron-sized functionalized poly(glycidylmethacrylate) adsorbent (F-PGMA) with polyaminophosphonic ligand for adsorption of two REs^{3+} typical for heavy REs (Y^{3+}) and light REs (La^{3+}). The physicochemical features are thoroughly described utilizing a variety of techniques. Additionally, the results of the nonlinear adsorption isotherm, kinetics, and thermodynamics, were studied and graphically simulated using MATLAB software. Furthermore, the type of reaction was determined as well as, the number of reactions was predicted. Finally, the competitive interactions and simultaneity La^{3+} and Y^{3+} adsorption behavior in an equimolar binary system was studied.

2. Materials and Methods

2.1. Adsorbent Preparation

Prior research described the thorough synthesis of the parent PGMA and the subsequent functionalization using poly (phosphonic amine) [3, 4, 9]. All other chemicals were obtained from Prolabo; they were used as received. More detailed information for the different materials used was displayed in Section A (see Supporting Information Section).

2.1.1. PGMA Preparation

To prepare the parent PGMA microparticles, the dispersion polymerization process was used [11]. Following the next procedure: the dispersion medium was made by combining 3 g of PVP K-30 with 90 mL of a 90% ethanol/water solution in a 250 mL four-necked flask. Following that, 10 g of the monomer phase (GMA) and 0.2 g of the 2,2-azobisisobutyronitrile (AIBN, polymerization initiator) were mixed together before being added to the dispersion medium. To eliminate the gas phase and dissolved oxygen, the mixture in the polymerization reactor was treated to 30 minutes of nitrogen gas bubbling. Subsequently, with mechanical stirring, the polymerization reaction was conducted at 70 °C in reflux for 24 h. Centrifugation was used to produce the PGMA microspheres, after that they had been properly washed with deionized water and ethanol. Afterwards, they were dried at room temperature under vacuum.

2.1.2. PGMA Functionalization

The polyaminophosphonic acid-functionalized PGMA was prepared through two sequential stages [4]. In the first one, the previously prepared PGMA microspheres (10 g) were suspended in ethanol (20 mL) followed by addition of diethylenetriamine (DETA, 12 mL), then the reaction mixture was stirred for 18 h under reflux. The aminated PGMA was collected and recovered through filtration and repeatedly washed. In the second stage, phosphorous acid (5 g) was dissolved in 100 mL of HCl/water solution (1:1, v/v) followed by addition of the aminated PGMA (1 g), the mixture was then heated and refluxed in a 200 mL three-necked flask supplied with dropping funnel, thermometer and condenser. The formaldehyde solution (20 mL) was added drop wisely during 1 h and the mixture was kept under reflux for the next 24 h [9]. The final product of functionalized adsorbent (i.e., polyaminophosphonated-PGMA (F-PGMA)) was collected via filtration and extensively washed with ethanol and water. Finally, the sorbent was dried for 24 h at 75 °C. The obtained F-PGMA was deeply characterized by XRD, FTIR, CHN, ZPC titration, TGA, and XPS techniques. More detailed information for the different characterization was displayed in Section A (see SIS).

2.2. Metal Adsorption and Desorption

A steady volume of aqueous solution (25 mL, C_o: 50 $mg.L^{-1}$) was added upon a functionalized

PGMA adsorbent mass (m: 0.01 g) to perform batch experiments. At room temperature (T: 25 ±1°C), the flasks were kept agitated for 24 h (agitation speed: 200 rpm). Phase separation was carried out, as well as the residual content (C_{eq}, mmol.L^{-1}) in the aqueous phase was calculated. Additionally, calculate the mass balance from the equation of metal concentration in the adsorbent (q_{eq}) that equals [(C_o-C_{eq})V/m], where the initial and final metal concentration denoted by C_o and C_{eq}, (mg.L^{-1}), respectively, as well as m(g) and V(L) are the weight of adsorbent and volume of aqueous metal solution, respectively. Meanwhile, the distribution coefficient K_d can be evaluated by the informatively of equilibrium ratio [q_{eq}/C_{eq}]. The influence of several parameters as: pH, uptake kinetics, adsorption isotherms, temperature, as well as, metal desorption and adsorbent recycle throughout the course of six successive adsorption and desorption cycles were studied to investigate of adsorption performance. The standard deviation was less than 7% and the experiments were repeated twice. The experimental steps of adsorption settings were achieved (pH:5.0, C_0: 200 mg.L^{-1}, V/m: 50 mL/20 mg, time: 180min, T: 25 °C). The metal analysis and mass balance estimation are performed before proceeding to metal desorption. The desorption step was completed, by contacting the collected adsorbent with HNO_3 (25 mL, 0.5 M) for 90 min at room temperature. The desorption efficiency (DE, %) (DE = C_D x $V_{(L)}$ x 100/q_d x m_d) and regeneration rate (RE, %) (RE = q_d x 100/q_e); where C_D (mmol.L^{-1}) is the RE^{3+}concentration in desorption solution, $V_{(L)}$ is the desorption solution volume, q_d (mmol.g^{-1}) is the adsorption capacity for metal loaded material before desorption experiment, q_e (mmol.g^{-1}) is the adsorption capacity at the first cycle, and m_d (g) is the amount of the adsorbent used in the desorption experiments. The adsorption yield after regeneration for six cycles was compared to the value reached for the first cycle.

3. Results and Discussion

3.1. Adsorbent Synthesis

Scheme 1 depicts the synthesis of PGMA and its subsequent functionalization using polyaminophosphonic acid to produce F-PGMA. To open the epoxide ring, diethylenetriamine and amino groups are grafted after the production of parent PGMA (micro-particles < 75 m) using the dispersion polymerization technique [3, 11]. Methylenephosphonic groups are eventually grafted to produce the transitional substance via the interaction of phosphonic acid groups onto amine functions by formaldehyde. When the methylene phosphonic group is added to the PGMA macromolecule together with phosphonic acid and formaldehyde, one or two phosphonomethyl moiety for polysubstituted structure, i.e., the grafted polymer may have both mono- and di-substituted amines (e.g. Polymer –NH–CH_2 –PO_3H_2 and/or Polymer –N(–CH_2 –PO_3H_2)$_2$), may be yielded [4, 9]. In order to identify these reactive groups, a number of analytical approaches have been employed.

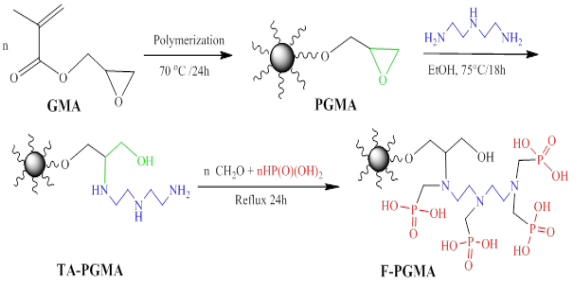

Scheme 1. Synthesis of functionalized polyglycidylmethacrylate: F-PGMA.

3.2. Adsorbent Characterization

3.2.1. Morphology and Textural Features

PGMA particles are depicted in a SEM picture in Fig. 1a. This illustration depicts large objects of erratic size. Assessing the distribution of particle sizes was made possible by the image-processing programme (Foxit PhantomPDF) (appearing in the same figure). A rough, unusual spherical form characterizes the particles. 52.92 ±6.61 µm is the estimated average particle size. The XRD patterns of natural and functionalized PGMA materials are displayed in Fig. 1b. The weak crystallinity of the PGMA substrate is consistent with the poorly resolved XRD patterns. There are different peaks which compatible with the XRD fingerprint of amorphous PGMA were appeared as: at 17.7°as a major peak, at 9.5-13°, 28-31°, and 40-44°; that characterized by weak and broad shoulders [9]. Although the overall structure is kept, the XRD peaks intensity and width display a relative reduction reveals that to the substitution of PGMA by diethylenetriamine and aminophosphonomethylation potentially enhances the disorder in the polymer structure (with detection of peaks at angles close to the values reported for pristine PGMA). N_2 adsorption/desorption isotherms have been used to investigate the textural properties of F-PGMA (Fig. 1c). The obtained information of the chemical reaction obeys to Langmuir categorization criteria for Type II isotherms. It is remarkable that the profile exhibits a mesoporous hysteresis loop, which is extremely weak. For single point and multipoint analyses, respectively, the specific surface area (S_{BET}: in $m^2.g^{-1}$) is roughly 24.96 and 50.54 $m^2.g^{-1}$ having approximately 2.52 nm as an average pore diameter. Furthermore, the pore volume was about 0.0438 cm^3. STP.g^{-1}. According to Wei et al. [16], PGMA has an S_{BET} of about 29 $m^2.g^{-1}$; the S_{BET} increased with the presence of divinylbenzene co-polymers. This order of magnitude is comparable with the reported values of SSA for PGMA.

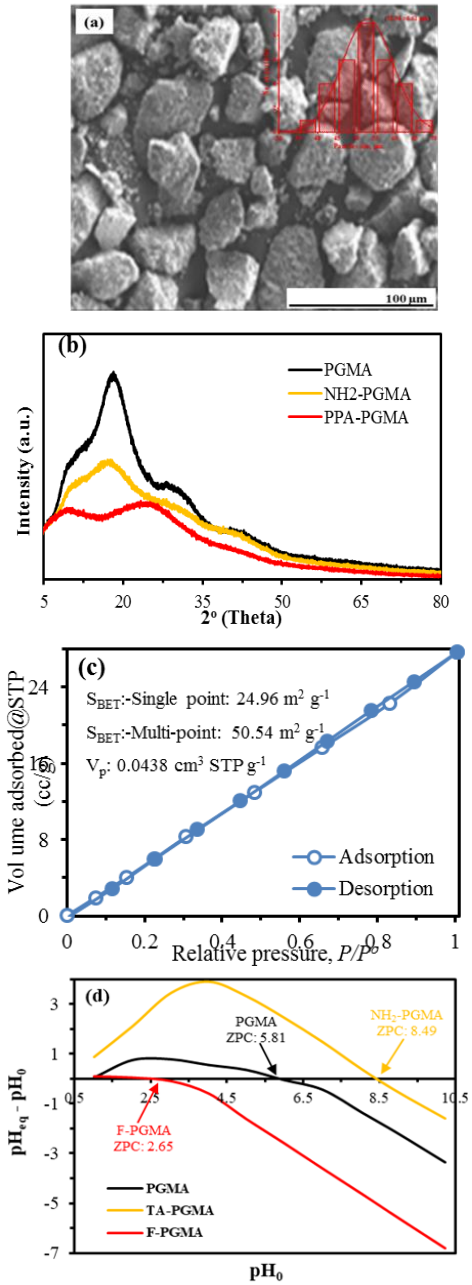

Fig. 1. SEM image and particle size analysis for PGMA (a), XRD patterns for PGMA, TA-PGMA and F-PGMA materials (b), Textural analysis of F PGMA–N2 adsorption and desorption isotherms(c), and ZPC analysis (d).

3.2.2. pH Zero-Point Charge (ZPC)

For the purpose of calculating the ZPC of PGMA, TA-PGMA, and F-PGMA, the pH-drift approach was employed (Fig. 1d). The subsequent chemical alterations have a significant impact on the acid-based characteristics of PGMA derivatives. As anticipated, adding DETA to the polymer (TA-PGMA) results in the addition of basic groups (i.e., amine groups) to the polymer; thus, the ZPC rises from 5.81 to 8.49 are directly associated with the amine groups pKa values in DETA, which are 3.58, 8.86, and 9.65 [18]. According to Chen et al. [19], ZPC value for wheat residue grafted with DETA was close to 5, which is significantly lower than the level attained with TA-PGMA. For DETA-functionalized graphene oxide, a closer ZPC value (i.e., 8.2) was observed.

Following phosphonomethylation, ZPC was significantly displaced, which indicates that the quantity of substitution is quantitative and that the majority of alkaline amine groups have vanished. The acid-base characteristics of aminophosphonic acids were analyzed, it was discovered that the second pKa_2 value was significantly higher than the stronger acid group (i.e., in the range 5-6), which has a pKa_1 value in the range of 0.5-1.5 (correlated with the -O group; that is, stronger than the acidity of carboxylic groups, which is in the range from 2.2 to 3) [20]. As a result of the internal hydrogen transfer between P-OH and amino groups, aminophosphonic acids exhibit a zwitterion action [20]. Consequently, the P=O group's electron-attractive interactions decrease the electron density surrounding the amino groups as well as lowers the pKa values of them. Sahni et al. [21] described the following mechanisms to breakdown of the various reactive groups by ES 467 ion-exchange resin (contains aminomethylphosphonic acid moieties) according to the pH values: i) at the value equals 1.0, amino groups and P-OH groups were protonated and partially deprotonated respectively ($R\text{-}CH_2\text{-}N^+H_2\text{-}CH_2\text{-}P{=}O(OH)(O^-)$),, and ii) at the value approaching 6, a complete deprotonated process of the hydroxyl groups on the phosphonate group were achieved ($R\text{-}CH_2\text{-}N^+H_2\text{-}CH_2\text{-}P{=}O(O^-)_2$). Otherwise, by increasing the value of pH to 11, a deprotonation process was occurred at the amine groups as well as all hydroxyl groups (anionic aminophosphonate compound: $R\text{-}CH_2\text{-}NH_2\text{-}CH_2\text{-}P{=}O(O^-)_2$). This matches with the titration profile for F-PGMA seen on Fig. 1d [4]. Therefore, the electrostatic attraction/repulsion of the adsorbent for charged metal ions (pure electrostatic effects) and for the competition of protons is predicted using this acid-base behaviour (chelation and ion-exchange properties). It undoubtedly that additional factors related to metal speciation, in addition to the protonation/deprotonation of reactive groups on the adsorbent, may have an efficient impact upon the adsorbent's affinity for metal ions.

3.2.3. Elemental Analysis

By contrasting the elemental analysis of the product (CHN analysis) at different synthesis stages, it is possible to track the PGMA chemical alteration (Table 1). According to the theoretical composition of PGMA, the polymer can be approached by the heptameric formula $(C_7H_{10}O_3)_7$, which results from the conversion of C, H, and N constituents weight percentages in molar units [7]. On the other hand, the immobilization of the polyamine enables the nitrogen content to increase to 12.46% since the reaction with DETA takes place (w/w or 8.90 mmol N/g)

(diethylenetriamine, DETA). By contrasting the theoretical fractions of DETA and TA-PGMA for nitrogen permit to evaluate the substitution degree was to be around 63%. In the presence of formaldehyde, the reactivity of phosphonic acid groups with amine functionalities performed the grafted methylene phosphonic groups onto the transitional product (TA-PGMA).

Meanwhile, in the (F-PGMA), the calculate weight percentage (P) was attained 4.9 % (i.e., 1.582 mmol P/g). Logically, in the performed materials (PGMA and F-PGMA), the C (42.85%) and N (12.46%) mass fractions (w/w) were observed a drastically reduced on matrix backbone with simultaneous manner according to the chemical grafting process to be 34.72% and 9.48% (w/w), respectively. Assuming the mechanism of phosphomethylation to follow the reaction described on Scheme 1, the amine groups can be grafted by either one phosphomethyl moiety on secondary amine, or two phosphomethyl moiety on primary amine. By simulating the grafting of 1 to 4 phosphomethyl groups on TA-PGMA, and the product's appropriate weight fraction of N in the result is 9.48%. This number is approaching to the computed value (i.e., 9.77%) for a derivative grafted with only one phosphonate moiety on the polymer backbone H_2PO_3:R-N ratio (actually the simulated value would be 1.67 P mole per mole of TA-PGMA). In F-PGMA, the N/P molar ratio is extremely close to 4.28, according to the chemical analysis. This demonstrates without a doubt that the replacement on amine groups is not complete.

3.2.4. FTIR Analysis

FTIR spectroscopy can be used to track the sequential chemical alteration of PGMA (after the grafting of DETA and the ultimate grafting of phosphonomethyl groups), as well as identification of the functional groups involved in metal binding. These modifications could be linked to the emergence, removal, or movement of identifying bands [22, 23]. Fig. 2a describes the development of FTIR spectra for the various synthetic materials, as well as for metal-loaded F-PGMA.

The following groups can be utilized to determine the polymer's fingerprint based on the structure of PGMA: (a) carbonyl groups υ(-COO^-) at 1718 cm^{-1} [24], and (b) the oxirane ring exhibiting vibrations as asymmetrical stretching and asymmetrical expansion, identified by the two packs that appeared at 843 cm^{-1} and 904 cm^{-1}, respectively

[11, 25, 26]. Meanwhile, an appeared peak approximately at the wavelength 757 cm^{-1} was identified to an existence of epoxy ring, as well as stretch vibrations of C–O were recorded at the wavelength from 1300-1100 cm^{-1}[27]. Furthermore, the FTIR spectrum of TA-PGMA following DETA-grafting is characterized with vanishing of bands indicative of the epoxy ring [4, 11], while at the wavelength of 1718 cm^{-1} is still discernible. These obtained results indicate that no significant alteration occurred to carbonyl groups after chemical modification through grafting. Moreover, from another point of view, there are two new bands were existing at the wavelength of 1561 cm^{-1} and 1629 cm^{-1} that can be associated with N–H bending modes in secondary and primary amines, respectively [12]. N–H groups cause additional poorly resolved alterations to be displayed at 3350 cm^{-1}. The dis-appearance of the peaks connected to the epoxy ring (at 904 cm^{-1}, asymmetric vibration of epoxy ring) [11] also supports the mode of grafting amine compound on PGMA. New P-based reactive groups are added to TA-PGMA during its final modification, which happens when it reacts with phosphorus acid in the existence of formaldehyde. The emergence of common bands confirms this, at 746 cm^{-1} υs(–P=O), at 932 cm^{-1} υs(P-O-C) [15, 28] or to P–OH [29], at 1045 cm^{-1} υs(P–O–R), and at 1244 cm^{-1} υs(P=O) [15, 30]. Consequently, the successful grafting of reactive groups based on phosphorus is confirmed by these novel peaks.

3.2.5. XPS Analysis

XPS spectroscopy is a helpful not only for better understanding the nature of the interactions between the metal ions and the adsorbent, but also for detecting the alterations in the polymer's chemical composition throughout the different synthesis stages [3]. As a result of DETA grafting onto epoxy groups, Fig. 2b demonstrates the chemical alteration of PGMA caused by the introduction of N-based reactive groups as well as P-based reactive groups (related to main amino groups' phosphonomethylation).

Table 1. Elemental analysis and ZPC values for PGMA, TA-PGMA, and F-PGMA

Material		C		H	N		P		O		ZPC
		(%)	$mmol.g^{-1}$	(%)	(%)	$mmol.g^{-1}$	(%)	$mmol.g^{-1}$	(%) *	$mmol.g^{-1}$	
PGMA	Aver.	57.8	48.13	7.29	0.28	0.2	0	-	34.63	21.64	5.81
	S.D.	0.03		0.07	0.05						
TA-PGMA	Aver.	42.81	35.65	7.71	12.56	8.97	0	-	36.92	23.08	8.49
	S.D.	0.08		0.09	0.03						
F-PGMA	Aver.	34.69	28.88	7.06	9.36	6.68	5.16	1.67	43.73	27.33	2.65
	S.D.	0.09		0.11	0.04		0.15				

*: obtained by difference to 100 % (w/w fraction); n.d.: not determined.

The adsorbent is distinguished by the establishment of typical bands of La and Y elements following contact with a binary Y^{3+}/La^{3+} solution. Fig. 2b displays the XPS survey for the PGMA, and F-PGMA before and after loading with Y^{3+} and La^{3+} mixture. The graph enables an identification of the various forms connected to P, O, and N elements in their various chemical settings. The repeated grafting of amine groups and phosphonate groups has almost no impact on the proportions of the various chemical groups correlated to C and O.

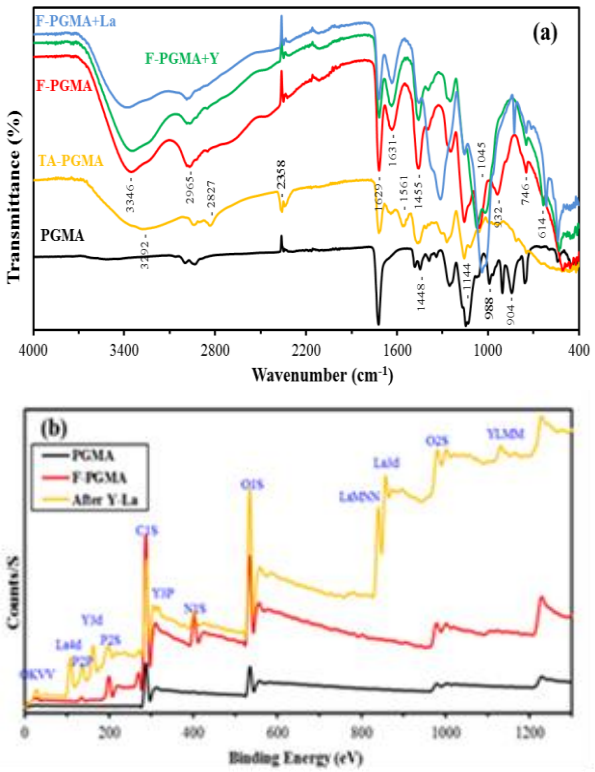

Fig. 2. FTIR spectra of PGMA, TA-PGMA and F-PGMA before and after La/Y adsorption (a) and XPS survey for the PGMA, and F-PGMA before and after loading with Y^{3+} and La^{3+} mixture (b).

The mild influence on the O1*s* signal could be attributed to the sparse substitution of phosphonate on amine groups; the only notable alteration is linked to a vital change in the BE of the peak at 534.7 eV. (Shifted toward lower BE; 534.2 eV). The identification of P-O, deprotonated, and protonated phosphonate groups is accomplished by the presence of weakly resolved peaks in the deconvolution analysis of the P2*p* signal. The electronic signal at different energies 402.9 eV and 400.8 eV recorded two deconvoluted peaks were existed, further supports both protonated and deprotonated amine groups existing together, respectively (at comparable atomic fractions). After metal adsorption, the chlorine element nearly completely vanishes from the adsorbent but is still detectable on F-PGMA (under two kinds and four deconvoluted peaks, likely related to protonation of amine groups and residual remains of absorbed chloride anions).

3.2.6. Thermal Properties

The chemical alteration of PGMA is proven by comparing the TGA and DTG profiles (thermogravimetric analysis and differential thermogravimetry), which reveal significant variations in the degradation profiles (Fig. S1, see SI). The PGMA TGA profile reveals multiple stages of deterioration, including (a) below 210 °C a plateau stage exhibited while stability occurrence through a slightly weight loss around 2-3 %, (b) between 210 and 344 °C a sharp weight loss was almost determined 70% at 320 °C on DTG curve, which approximately matches with PGMA's typical TGA thermogram [31]. As well as at the temperature of 301 °C produced the highest deterioration rate. Random chain scission is thought to be responsible for the degeneration. (c) in the range between 344 and 440 °C PGMA loses from its total weight approximately 97%, which consistent with the degradation of the polymer's shorter chains leading to the creation of a small amount of char (less than 3%). (d) finally, above 440 °C and up to 825 °C a complete degradation stage was accomplished, where PGMA is gradually loses the remaining char fraction.

Because F-PGMA contains novel organic chains with both amine and phosphonic groups, the thermal degradation profile is more complicated in this case: i) hydrophilicity of the modified polymer enhanced at temperature range from 25 and 65 °C releasing absorbed water (weight loss represents less than 14%). ii) slightly weight loss of roughly 3%, perhaps due to the release of constitutive water, and a stable plateau between 65 and 230 °C (or more tightly bound to polymer chains). (iii) sharp decrease of weight is observed between 230 and 320°C approximately 38%, with a maximum loss rate at 274 °C appeared in DTG curve may be attributed to degradation of the adsorbent through polymer scission as well as amine chains. (iv) degradation of phosphonate moieties and char formation in the range between 320 and 430 °C, and a new weight loss equating to 21% is observed. (v) gradually degradation of the char is observed in the range of 430 °C and up to 925 °C, however, the residual proportion of solid is 13% (w/w) even at 925 °C. By enhancing char formation and partially suppressing polymer scission, phosphorus-based compounds are commonly employed as char-forming additives for flame-retardant qualities [34]. Improvements in char formation, water absorption, and thermal stability are all results of the chemical alteration (lower slope of weight loss and increased residual solid). The degradation profiles further demonstrate that, in comparison to raw PGMA, the thermal degradation starts at a lower temperature (shift of about 30 °C).

3.3. Metal Interaction Mechanism

3.3.1. FTIR Analysis

The bands' intensities start to decline after the binding of Y^{3+} and La^{3+} at 3357 and 2966 cm^{-1}, respectively. Consequently, the environment of the OH and NH groups is changed as a result of the metal ions binding, which is directly responsible for these modifications (overlaying the pertinent, inadequately resolved bands). The obtained spectrums before and after Y^{3+} adsorption were comparable except for some differences and are summarized as follows: i) the blue shift of the band at 503 to 531 cm^{-1}, which relates to the Y-N bond, as well as 1045 cm^{-1} shifted to 1074 cm^{-1}, ii) the peak at 932 cm^{-1} that corresponds to P-O-C stretching was vanished, and iii) a new peak at 633 cm^{-1}, which is typically linked to the creation of the Y-O bond, and the development of a peak at 1018 cm^{-1} [30]. While as, the peak at 1250 cm^{-1} does not have a substantial impact by Y^{3+} adsorption, however Popa et al. [30] reported that the bands at 1050 cm^{-1} and 1250 cm^{-1} were blue-shifted in the case of Cu(II) and Mn(II) binding to aminophosphonate-based ligands (P=O and P-O-C bonds). On the other hand, concerning La^{3+} adsorption, the alterations are significantly more noticeable as follows: i) shift of the band at 506 cm^{-1} to 529 cm^{-1}, which relates to the La-N bond, ii) the appearance of peak at 633 cm^{-1} corresponding to La-O bond formation, as well as a new peak was noticeable at 826 cm^{-1} related to La-C=O bond, iii) the peak at 932 cm^{-1} was vanished, iv) A prominent peak was displayed at 1310 cm^{-1}, which is the specified region corresponding to C-N stretch vibration in amines [28]. as well as the peak at 1250 cm^{-1}correspond to the blue-shift of the P-O-C bond on the adsorbent. Whatever the case, the chemical environment around N- and P- reactive groups is significantly impacted by the binding of La^{3+}. The band that was detected at 1050 cm^{-1} (P=O) is redshifted to 1038 cm^{-1} and experiences a significant intensity boost following lanthanum binding. At the range between 400-800 cm^{-1} in the FTIR spectrum demonstrated a specified M-OH vibrations and O-M-O stretching bands that characterize LDH (layered double hydroxide) intercalated biopolymer nanocomposites [32].

3.3.2. XPS Analysis

Metal-related bands' interpretations demonstrate the coexistence of numerous metal styles where Cl, OH, and P-O- groups are most likely associated. Also, the appearance of La3$d_{5/2}$ peaks on Fig.S2 were displayed in the form of two multiplet-split couples with energies of 836.2/839.9 and 837.9/841.7 eV, respectively. As well as both $La(OH)_3$ and $La_2(CO_3)_3$ were appeared at energies 3.9 and 3.5 eV, respectively, recording an energy gap (ΔBE) closed to 3.7 eV. Moreover, alterations that appeared on O1*s* and P2*p* signals may be related to phosphonate-La^{3+} formation, while the other may be linked to chloride (see below). On the other hand, HCl was utilized to adjust the pH, which was also used to produce stock solutions. Other species could coexist, nevertheless, due to the very tiny atomic fraction of chloride. In addition, interactions with amine groups may result in the formation of hydroxo or hydroxo-chloride complexes, or the BEs may remain the same while the percentage of free amine groups increases after metal sorption. On the other hand, deconvolution of the spectra for Y3*d* signals reveals 6 peaks, 3 pairs (Y3$d_{3/2}$ and Y3$d_{5/2}$ bands) associated with chloride species (with the greatest binding energies) and phosphonate species. It's interesting to observe that the adsorption of metal ions causes the P–O peaks to move toward lower BEs with greater electronic density as well as lower relative intensity, also BEs for phosphonate groups are relatively stable, and the intensity of protonated and deprotonated phosphonate is simultaneously increasing and decreasing, respectively. Consequently, metal adsorption for the P–O group primarily affects the chemical environment of the O element, by shifting the BE from 531.8 eV to 530.8 eV, since the intensity falls at the same time. The O relative intensities altered significantly, whereas other signals are not altered in terms of BEs (i.e., C-O-C increased as well as C-OH and P-OH decreased). These findings are in agreement with FTIR analyses and show how phosphonate groups contribute to metal binding through the coexistence of various complexes or through various interactions with the nearby reactive groups.

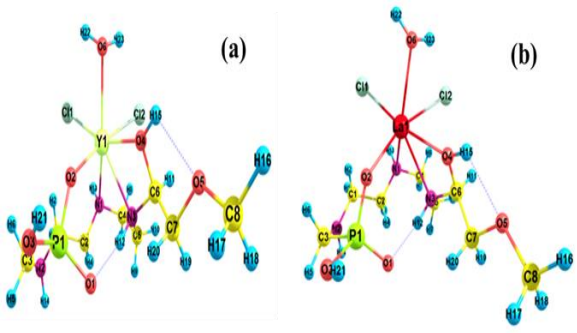

Scheme 2. Possible structures of Y^{3+}(a) and La^{3+}(b) complexes in F-PGMA with aminophosphonate moieties.

3.4. Linear Adsorption Studies

Batch adsorption studies were carried out to assess the capability of F-PGMA to adsorb REs^{3+} as (Y^{3+} as well as La^{3+}) through the following parameters:

3.4.1. Effect of pH

The pH factor had a substantial impact upon the metal ions' ability to bind to F-PGMA in a batch adsorption experiment with metal ions like

($[Y^{3+}/La^{3+}]_0$ ~75 mg.L^{-1}) at varied pH levels from 1.0 to 6.0 for 12 h at 25 ºC . Due in major part to the positively charged surface of the F-PGMA, which repels metal cations by repulsion force, the F-PGMA demonstrated a low adsorption when the pH is below 2. Otherwise, the decline in adsorption capacity is brought on by REs^{3+} and H^+ ion competition at the various active centers of adsorbent. The H(I) ion has a significant adsorption competition due to its small size [10, 33]. Whilst, Y^{3+}/La^{3+} adsorption capacity considerably enhanced when the pH value was higher than 3.0 and until reach 6.0. The highest capabilities of adsorption in mmol.g^{-1} were achieved at pH_0 equals 5.0 in the La^{3+} (0.608) > Y^{3+} (0.540) followed by a small increase for both (Fig. 3a). This is probably because of the free metal ion exchange or interact with F-PGMA active sites [34]. Therefore, the pH_0: 5.0 were selected for further studies.

In case of the pH_0 value was higher than ZPC value, the metal–ligand interaction agrees with the ZPC-values because of the deprotonation process were accomplished through the reactive groups as: hydroxyl, phosphonate, as well as amino groups in different materials [15]. Therefore, the repulsion decreases, the ability to coordinate with sorbents improves, and the capacity for adsorption increases [35, 36]. The pH_0 fluctuation following metal ion adsorption is shown in Fig. S3. At pH_0: 3.0 to 6.0, the pH changed dramatically and tended to decline: the pH stabilizes at 3.3 for La^{3+} and 3.4 for Y^{3+}. The pH_{eq} did not vary between pH_0: 1.0 and 2.0. Consequently, the acid-base properties of F-PGMA are consistent with this "buffering effect"[15]. In Fig. 3b, the distribution ratio (D: q_{eq}/C_{eq}, L/g) is plotted as a logarithmic function of pH_{eq}. The linear relationship between the $\log_{10}D$ plot and pH_{eq} is caused by the stoichiometric anion/cation exchange with bounded metal species during the ion-exchange reaction [10], achieving slope with approximately values 0.4605 and 0.5996 for Y^{3+} (R^2:0.9073) and La^{3+} (R^2: 0.9283), respectively. As illustrated in Scheme 2, the ion-exchange mechanism is significantly controlling the adsorption process as indicated by the good correlation coefficient for all ($R^2 > 0.91$) [12, 15].

3.4.2. Effect of Contact Time and Linear Kinetic Studies

F-PGMA was connected with Y^{3+}/La^{3+} at a concentration of ([M]~200 mg.L^{-1}) to study the adsorption kinetics. Comparisons was made between the adsorption uptake kinetics (Fig. 3c) according to the reaction time as follows: i) within the first 15 min for Y^{3+}/La^{3+}, the adsorption kinetics is quite quick, reaching roughly 32% and 43% respectively. ii) after 180 min, between 93.2% for La^{3+} and 99.8% for Y^{3+} from the total capacities were reached. After that, Y^{3+} demonstrated a slower adsorption followed by adsorption equilibrium over the next 180 min, whereas La^{3+} took 240 min. The adsorption capacity was finally arranged and attained q_e, in mmol.g^{-1} at 0.790 (La^{3+}) > 0.739 (Y^{3+}), suggesting that F-PGMA is an effective adsorbent.

To comprehend the dynamics of better adsorption, the adsorption data was examined as a function of time with the mathematical equations in Table S1, (see SI) [37]. using three models as follows: i) the pseudo-first-order kinetic (PFO), ii) pseudo-second-order kinetic (PSO), and iii) intra-particle diffusion models [9, 10]. Furthermore, by using the kinetic models to fit the experimental adsorption data, the parameters of these kinetic models may also be discovered. The kinetic parameters are listed in Table 2.

Comparing the predicted and experimental adsorption capacities (q_e, Table 2) revealed that the experimental data achieved a best fitting to the PSO kinetic model, in contrast to the PFO data, which highly underestimated values (14.8-23.7%), while, the PSO model differences slightly overstated values (4.60-8.6%). Moreover, the correlation coefficient also arranged as follows: PSO > R^2 (0.99) > PFO. Consequently, chemical adsorption is anticipated to be the phase that determines rate [36, 38], since the experimental data best support the PSO. According to Kyzas et al. [39], the faster appears to be the case when comparing the apparent rate coefficients for PSO (k_2, mmol.g^{-1}.min^{-1}). Consequently, these values roughly fall into the same order:

Table 2. Kinetics and isotherm adsorption parameters

			PFO			PSO			sRIDE		
Kinetics models	Metal ion	$q_{m,exp.*}$	$K_1\times10^{-3}$ (min^{-1})	$q_{e,1.*}$	R^2	$K_2\times10^{-3}$*	$q_{e,2}^{*}$	R^2	$K_{id,1}^{***}$	$K_{id,2}^{***}$	$K_{id,3}^{***}$
	La^{3+}	0.79	14.28	0.673	0.9899	39.79	0.858	0.9919	0.0722	0.0416	0.0001
	Y^{3+}	0.739	21.19	0.605	0.9851	79.15	0.779	0.9972	0.0784	0.0298	0.0003
			Langmuir isotherm			Freundlich isotherm					
Isotherms models	Metal ion	$q_{m,exp.*}$	$q_{m,L.*}$	b_L, L.mmol^{-1}	R^2	n	k_{F*}	R^2			
	La^{3+}	0.789	0.818	13.0149	0.9987	6.84	0.7310	0.9730			
	Y^{3+}	0.736	0.774	5.1523	0.9980	4.94	0.6012	0.9375			

Units: *: mmol.g^{-1}, **: g.$mmol^{-1}$.min^{-1}, and ***mmol.g^{-1}.$min^{-0.5}$

The quicker adsorption equilibrium is confirmed by the fact that Y^{3+} (79.15×10^{-5}) > La^{3+} (39.79×10^{-5}).

It was also possible to calculate the half-sorption time ($t_{0.5}$), which is the amount of time needed for the adsorbents to reach 50% of their maximal sorption capacity according to the given k_2 values. As stated ($t_{0.5}= 1/k_2.q_2$), the $t_{0.5}$ could be utilized as a measure of the adsorption rate [12, 15], however, it was equals to 16.2 min for Y^{3+} and 29.3 min for La^{3+} in agreement with the k_2 and experimental findings. Hubbe et al. [40] stated that, the PSO's profiles fitting indicates that an intraparticle diffusion regulates the adsorption process. A multi-linear plot with three main stages (initially, external surface adsorption, and gradual adsorption stage), the Weber and Morris plots were utilized to evaluate the sRIDM for rate control activities in the adsorption process (Table 2 & Fig. S3, see SI) [46]. This implies that the adsorption rate is influenced by an intraparticle diffusion as well as the boundary layer. The adsorption segment is the final and is almost saturated [35, 41, 42].

3.4.3. Linear Adsorption Isotherms

Y^{3+}/La^{3+} adsorption were examined as a function of initial metal concentration at ($[M]_0$ ~26-400 mg.L^{-1}) and pH_0 value equals 5.0 for 3/4 h, to assess adsorbent capabilities. The adsorption equilibrium results are demonstrated in Fig. 3d. As initial and equilibrium metal concentration increased, the equilibrium adsorption capacity grew dramatically and appeared to be steady above approximately 200 mg.L^{-1}. This is most likely caused by the F-PGMA surface's adsorption site saturation [36, 38], and the the maximum adsorption capacity ($q_{m,exp}$ in mmol.g^{-1}) of F-PGMA was achieved 0.74 and 0.79 for Y^{3+} and La^{3+}, respectively.

The F-PGMA displayed competitive adsorption capacity performance when compared to other adsorbents, this is caused by the abundance of its active sites, the enormous F-PGMA surface areas, and the strong attraction of aminophosphonic groups for metal ions. An empirical theory called the Langmuir isotherm makes the assumption that monolayer adsorption takes place on a homogenous surface. However, the adsorption process that takes place on a heterogeneous surface is typically described using the Freundlich model [36]. Therefore, Freundlich and Langmuir isotherm linear models were used to match the adsorption data in order to comprehend the adsorption mechanism of F-PGMA for metal ions [37]. In terms of correlation coefficient (R^2) values, the isotherm data suited the Langmuir better than the Freundlich model. Additionally, the hypothesized adsorption capabilities and the actual measurements were in good agreement with Langmuir model that achieving $\Delta q_{m,cal}$.=3.71-7.32%, otherwise Freundlich model exhibiting $\Delta q_{m,cal}$.=7.36-18.28%. Consequently, the obtained data imply that an ion monolayer has formed on the F-PGMA surface (Fig. S5 and Table 2).

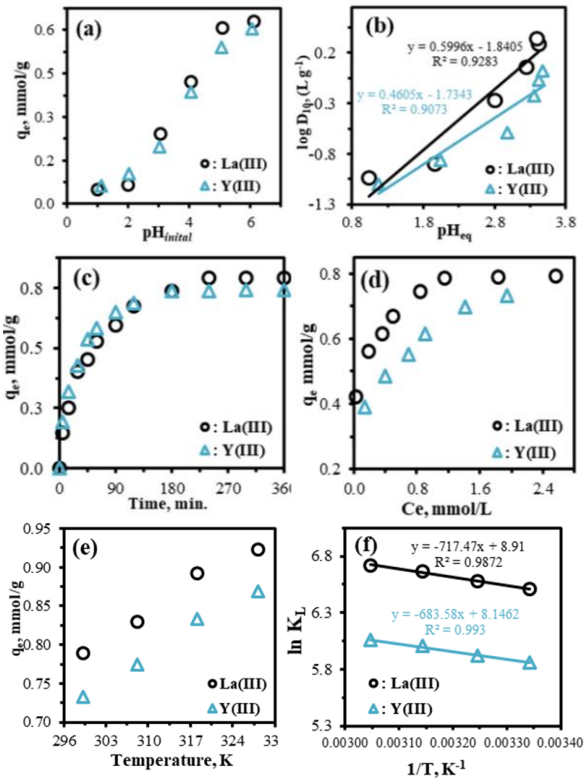

Fig. 3. Effect of pH: q_e vs. $pH_{initial}$ (a), Plot of logD_{10} vs. pH_{eq} (b), adsorption kinetics (c), adsorption isotherms (d), temperature effect (e), and Thermodynamics of adsorption–Van't Hoff plots of ln b_L vs 1/T (f).

3.4.4. Linear Adsorption Thermodynamics

The thermodynamic characteristics of Y^{3+}/La^{3+} adsorption were examined at pH_0: 5.0 and $C_{0:}$ 200 mg.L^{-1}, the adsorption capabilities were tested at four different temperatures ranging from 299 to 328 K. (Fig. 3e).

Table 3. Thermodynamic parameters of metal ions adsorption

Metal	La^{3+}					Y^{3+}				
T, K	ΔH^o (kJ.mol^{-1})	ΔS^o (J.mol^{-1}.K^{-1})	ΔG^o (kJ.mol^{-1})	$T\Delta S^o$ (KJ.mol^{-1})	R^2	ΔH^o (kJ.mol^{-1})	ΔS^o (J.mol^{-1}.K^{-1})	ΔG^o (kJ.mol^{-1})	$T\Delta S^o$ (KJ.mol^{-1})	R^2
299	5.97	74.08	-16.20	22.16	0.987	5.68	67.73	-14.58	20.26	0.993
308			-16.86	22.83				-15.19	20.87	
318			-17.60	23.57				-15.86	21.55	
328			-18.34	24.31				-16.54	22.22	

Enthalpy (ΔH^o, kJ.mol^{-1}) and entropy (ΔS^o, J.mol^{-1}.K^{-1}) changes were calculated using the Van't Hoff equation, as follows: lnD = (-H°/R) 1/T + S°/R, whereas the free energy change ($\Delta G°$, kJ.mol^{-1}) was derived from $\Delta G° = \Delta H° - T\Delta S°$) [43, 44], as well as at each temperature, the distribution coefficients (D: q_{eq}/C_{eq} in L.g^{-1}) after corrections and unit conversion (L.g^{-1} to L.mol^{-1}) were calculated and processing with no dimensions (adjusting for molality in the water) according to Lima et al. [43].

An acceptable fit of the experimental data is made between the thermodynamic parameters listed in Table 3 and the linear plots of ln*D* vs. 1/T. (Fig. 3f).

The thermodynamic parameters were evaluated as follows: i) The absolute ΔH°, which provide evidence that the process is endothermic according to its positivity (ranging from 5.68 to 5.97 kJ.mol^{-1}) exhibit favourable implications irrespective of the cation type, as the higher temperatures make the process more advantageous. ii) The absolute ΔS°, which support the randomness of the chemical reaction, by its positive value that evaluated between 67.73 and 74.08 J.mol^{-1}.K^{-1} as a sign of increased randomness after F-PGMA-metal interaction at the solid-liquid boundary [45]. iii) The absolute ΔG°, which express the spontaneity of the chemical reaction, its negative values from -14.58 to -18.34 kJ.mol^{-1} demonstrated spontaneous manner of the system [12, 46]. Table 3 shows that, entropic rather than enthalpy changes influence the reaction ($|\Delta H°| < |T\Delta S°|$) [15].

3.4.5. Adsorption with Preference

Both equilibrium and dynamic experiments demonstrate that, the F-PGMA has relatively comparable adsorption capabilities for both elements heavy (Y^{3+}) and light (La^{3+}) REs. Separating individual element looks challenging particular for REs. A binary solution with equimolar concentrations, was used for further and additional experiment: (~1.0 mmol.L^{-1}) for heavy RE (Y^{3+}: ~89.0 mg.L^{-1}) and light RE (La^{3+}: ~138.99 mg.L^{-1}).

After equilibration, the adsorption capacities are ~0.57 and ~0.36 mmol.g^{-1} for La^{3+} and Y^{3+}, respectively. The molar ratio of Y^{3+}/La^{3+} in the solution was initially ~1.0; after metal adsorption, it increased to 1.12 in the adsorbent. Fig. 4 shows the molar ratios (in relative percentage, %) of the bi-metal ions in the aqueous solution, treated raffinate as well as the F-PGMA adsorbent's surface. Notably that, the solution had significantly changed before and after treatment. It is the first evidence that Y^{3+} and La^{3+} had a minor differential and concentration impact in the adsorbent. When comparing the metal ions on the adsorbent surface, La^{3+} represents about 61.0% (~0.57 mmol.g^{-1}) of the entire adsorption capacity (0.93 mmol.g^{-1}), while Y^{3+} was enhanced and enriched in the raffinate solution. However, to achieve metal separation, would have needed multiple enrichment processes and these changes were not very noticeable. The overall adsorption capacity was about 0.93 mmol.g^{-1}, which is slightly higher and close to the highest adsorption capabilities discovered for the La^{3+} binding

.

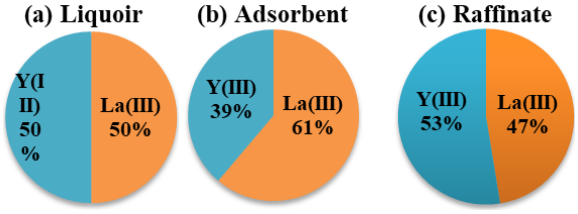

Fig. 4. The proportion of the bi-metal ions in aqueous solution (a), F-PGMA surface (b), and raffinate after treatment (c).

3.4.6. Metal-desorption and Recycling

Costs associated with metal recovery can be significantly decreased if adsorbent material can be effectively reused over many adsorption/desorption cycles [36]. To test F-PGMA efficiency, capacity and durability for reused repeatedly, it was equilibrated with Y^{3+}/La^{3+} solutions and then desorbed by HNO_3 solution (0.5 M). The F-PGMA is reusable with a high efficiency in metal adsorption capacity throughout six reuse cycles, indicating its strong stability and simple regeneration approach. The adsorption and desorption efficiencies are greater than 93% (Table 4). After six cycles, the adsorption and desorption efficiencies were 93.4 and 94.2%, for La^{3+} and 95.2 and 95.3% for Y^{3+}, respectively.

Table 4. F-PGMA adsorption/desorption efficiencies

Cycle no.	La^{3+}		Y^{3+}	
	Adsorption, %	Desorption, %	Adsorption, %	Desorption, %
1	100.0*	97.75	100.0*	98.25
2	96.79	97.22	97.69	98.02
3	96.26	96.68	96.93	97.92
4	94.96	95.73	95.58	96.98
5	94.05	94.91	93.12	96.04
6	93.41	94.24	95.20	95.35

* Based on the efficiency of first adsorption cycle

3.5. Nonlinear Adsorption Studies in 3D

The equilibrium uptake of Y^{3+} and La^{3+} can be affected by numerous variables; the most important one is the pH factor that has a direct impact upon the adsorption process, also the initial concentration of metal ions as well as contact time are another considerable factors in the adsorption process that impacts the process's economic efficiency and the adsorption kinetics[47]. On the other hand, the solution temperature has a huge influence to change the nature of adsorbents causing expansion of its particles followed by mobility alteration of adsorbate

ions and the solid/liquid interface, which controlled the rate of reaction within its vital role to describe the type of an exhibited interaction. To understand the Y^{3+}/La^{3+} adsorption behaviour, the chemical reaction must be reached to the equilibrium state for each factor affecting the reaction [8]. The experimental results are fitted with the generalized non-linear Langmuir isotherm model; therefore, the theoretical studies will be started by applying the nonlinear model of Langmuir in this section (Table S1) [4, 47].

3.5.1. The Relation between Initial Metal Ion Concentration and Initial pH

With the generalized non-linear Langmuir model via simultaneous variation of initial pH and initial concentration of Y^{3+}/La^{3+} against the equilibrium uptake (q_e in mmol.g^{-1}); MATLAB simulates this relation in 3D (Fig. 5) [15, 47]. The suggested model clarifies the maximum uptake which represented to the adsorption process capacity, and it can be calculated from Eq. (1) for La^{3+} and Y^{3+} (~0.79 and ~0.74 mmol.g^{-1}, respectively), as well as the Langmuir constants (b_L) were evaluated as 93423.25 and 31203.02 L.mmol^{-1}, respectively. The simulated powers (e, f, g, m, and n) that verified the suggested model showed in Table 5. Also, the free energy of this system can be estimated from Eq. (2), was found to be -28.465 and -25.738 kJ.mol^{-1} for La^{3+} and Y^{3+}, respectively, these values are in agree with the experimental results.

This confirm the well-fitting with the mathematical model.

$$q_{(pH,C_0)} = \frac{q_m \times pH^m \times C_0^n}{(1+k\times pH^f \times C_0^e)^g} \quad (1)$$

$$DG = -8.314 \times 299.15 \times log e^{K/1000}/1000 \quad (2)$$

Fig. 5a confirms a good accuracy to describe a single component adsorption on the F-PGMA using the Langmuir equation. These different probabilities relations clarify that the adsorption process was affected by the initial concentration than the equilibrium pH for La^{3+}, on the contrary for Y^{3+} adsorption (i.e., the initial pH is more effective than the initial concentration) [15].

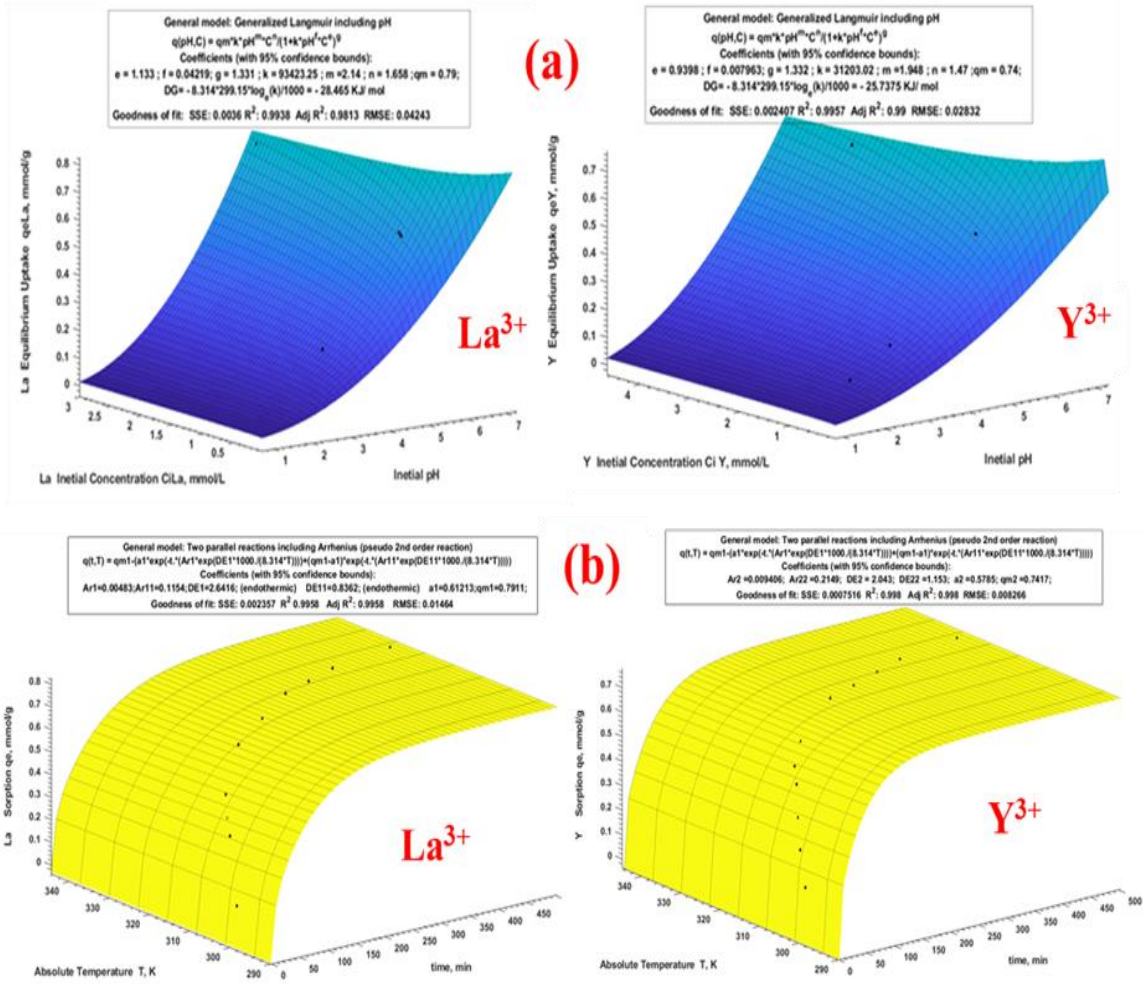

Fig. 5. Generalized Langmuir including pH and C_0 (a) and two parallel reactions including Arrhenius in PSO reaction (b).

3.5.2. The Relation between Equilibration Time—Temperature

Modeling of experimental kinetic data provides a description of the uptake mechanisms and phenomena that control the adsorption process. Fig. 5b displays the Time-Temperature findings response to adsorption capacities graphed in 3D space of extended relationships. The applied nonlinear fitted equation of the PSO including Arrhenius was expressed as a function of time dependent temperature Eq. (3) [47].

q(t,T)=qm1-(a1*exp(t.*(Ar1*exp(DE1*1000./(8.314*T))))+(qm1-a1)*exp(t.*(Ar2*exp(DE2*1000./(8.314*T))))) (3)

The suggested model Eq. (3) predicted that there are two chemical reactions were occurred following- in total- the PSO model including Arrhenius (Fig. 5b) with a satisfactory coefficient of determination [15]. Fig. 6 displays all parameters (Table S2). The easier adsorption kinetics is, the lower the Ea (activation energy). Notably, Ar_2 > Ar_1 for both elements (La^{3+}/Y^{3+}) confirms the suggested claim: that chelation mechanism is a quicker process than ion-exchange one [15].

The level in which the mathematical findings coincide with the experimental results is measured by the error percentage (Error (%)=(($q_{e,exp.}$-$q_{e,Calc.1}$)*100))/$q_{e,exp.}$), which is used to assess the validity of the mathematical technique. The results of the mathematical equation's validation and comparison are shown in Table 6. The accuracy and reliability of the mathematical approach is evaluated, and found that it is at maximum ±10.826 %. The calculated uptake correction of La^{3+} and Y^{3+} were evaluated, by applying the general model of sin3 and Gauss3, respectively using the MATLAB software, that achieved more fitting with lesser error ±2.858 % (Eq. 4, 5) (Table 6).

For La^{3+}: q_t,cor = a1*sin(b1*x+c1) + a2*sin(b2*x+c2) + a3*sin(b3*x+c3) (4)

For Y^{3+}: q_t,cor= a1*exp(-((x-b1)/c1).^2) + a2*exp(-((x-b2)/c2).^2) +a3*exp(-((x-b3)/c3).^2) (5)

3.5.3. Determination of Reaction Type

Modeling of experimental data for the heterogeneous reactions is commonly used since Levenspiel 1999 postulation of a new model known as a shrinking core model [17]. The main function of the shrinking core model utilization is to determine the type of the occurred reaction from its mechanism. There are three different controlling mechanisms were happened; i) diffusion control through a product layer, ii) surface reaction control, and iii) diffusion control through liquid film layer [48] as following in Eqs (6–8), respectively.

$$t = k_D.t = 1 - 3(1-x)^{\frac{2}{3}} + 2(1-x) \quad (6)$$

$$t = k_c.t = 1 - (1-x)^{\frac{1}{3}} \quad (7)$$

$$t = k_f.t = x \quad (8)$$

where, t is the reacted time, kc is the reaction rate constant, and X is the fraction of particle reacted.
The value of kc used in the subsequent computation, which is derived from the best model and yielded the greatest determination coefficient (R^2), was used to identify the reaction mechanism. The predicted non-linear model was fitted from the 3D relation of Xf(q_t/q_m) against time and absolute temperature (Fig. 6a) as in Eq. (9). According to Table 6, the reaction constant values for both elements follow the pattern $k_C > k_D < k_f$, with an R^2 value (0.996/4) (TableS2), indicating that the reaction is being regulated by a solid diffusion reaction[17].

Table 6. Adsorption capacity (qe) comparisons using experimental and mathematical data (qe) and correlation factors for the two parallel reactions including Arrhenius (PSO) for both La^{3+} and Y^{3+}.

Metal ion		La^{3+}					Y^{3+}				
t (min)	T (K)	$q_{e,exp}$	$q_{e,calc}$	Error%	$q_{e,cor}$	Error%	$q_{e,exp}$	$q_{e,calc}$	Error%	$q_{e,cor}$	Error%
5	299	0.146	0.141	3.947	0.143	2.100	0.193	0.192	0.529	0.194	-0.170
15	302	0.251	0.278	-10.826	0.258	-2.858	0.321	0.320	0.173	0.320	0.126
30	304	0.402	0.384	4.535	0.389	3.194	0.427	0.434	-1.629	0.428	-0.122
45	307	0.454	0.459	-0.987	0.472	-3.751	0.537	0.516	3.881	0.536	0.239
60	310	0.530	0.518	2.204	0.521	1.744	0.584	0.576	1.350	0.585	-0.319
90	312	0.594	0.607	-2.147	0.596	-0.301	0.648	0.652	-0.528	0.644	0.620
120	315	0.675	0.666	1.280	0.666	1.345	0.685	0.692	-1.021	0.692	-1.024
180	318	0.736	0.734	0.349	0.752	-2.181	0.739	0.727	1.607	0.731	1.091
240	320	0.790	0.764	3.274	0.781	1.185	0.739	0.737	0.218	0.739	-0.058
300	323	0.791	0.778	1.536	0.789	0.223	0.740	0.740	-0.105	0.741	-0.256
360	326	0.791	0.785	0.755	0.791	-0.016	0.741	0.741	-0.043	0.742	-0.151
480	328	0.791	0.790	0.161	0.792	-0.148	0.742	0.742	-0.001	0.742	-0.090

However, k_C is a function of the rate constant of the chemical reaction, k_D is a function of the rate constant of the solid diffusion reaction, and k_f is a function of the rate constant of the film diffusion reaction. Herein the solid diffusion reaction has a crippling effect to the rate of reaction consequently, to overcome that effect must decrease the adsorbate (La^+ and Y^+) size, increase the surface area and/or increase the porosity of adsorbent and increase speed of agitation.

*f(Xf,T)=((1/kf)*Xf+(1/kD)*(1-3*(1Xf).^{(2/3)}+2*(1-Xf))+(1/kC)*(1-(1-Xf).^{(1/3)})*(exp(Ar1*exp(E1*1000/(8.314*T)))+exp(Ar2*exp(E2*1000/(8.314*T)))))* (9)

3.5.4. Vermeulen model

Most of the time, the experimental data of adsorption can be fairly well reconstructed by the Langmuir, Freundlich, ….etc. for adsorption of single components as well as applying LeVan–Vermeulen model for multicomponent mixture adsorption [17]. LeVan and Vermeulen considered the thermodynamic inconsistencies of the competitive Langmuir model and improved the model using the ideal adsorbed solution theory (IAST) model. The multicomponent competitive isotherm equation developed by LeVan and Vermeulen takes into account the various capabilities of the dissolved substances in the mixture [49]. The validity of this model depends on whether the pure component exhibits the Langmuir isotherm.

As shown below is the general LeVan and Vermeulen Eq. 10 [50]:

$$q_{e,i} = \frac{q^*_{m} K_i C_{e,i}}{1+\sum_{j=1}^{N} K_j C_{e,i}} + C_{e,i}\left(\frac{\partial q^*_m}{\partial C_{e,i}}\right) ln\left(1+\sum_{j=1}^{N} K_j C_{e,i}\right) \quad (10)$$

$$q^*_m = \sum_{i=1}^{N}\left(\frac{q_{m,i} K_i C_{e,i}}{K_i C_{e,i}}\right)$$

The q_m* value was evaluated from,

where, q_m, and K_i are maximum amount of adsorbate adsorbed, and adsorbate–adsorbent affinity constant for component i, respectively.

During the adsorption process in the binary system, the metal ions were equimolar prepared, so the interaction is described by the ratio of the maximum capacity of adsorption (q_m) to the equilibrium one (q_e), which is represented by three cases: i) If $q_m/q_e < 1$ the adsorption behavior is known by an antagonism nature, ii) If $q_m/q_e > 1$, the adsorption process behavior is recognized as synergism behavior, iii) If $q_m/q_e=1$, that means there is no effect of the mixture so the adsorption behavior is non interactive[17]. Inglzakis and poulopoulos reported that Helfferich 1962 made an approximation for the Vermeulen equation. This approximation after that was deployed successfully and sounded as Vermeulen equations for 1st and 2nd order. The suggestion of mixing fits this system efficiently as shown in Fig. S6

Fortunately, in this work, the occurred adsorption process achieved with a synergism behavior. The applied modified Vermeulen model achieved a well fitting which expressed a mixed behavior of reaction as in Eq. (11) as follow:

f(t)=(a(1-exp(-k1*x))+(1-a)*((1-exp(-k2*x)))^0.5* (11)

where, a is the fraction of Vermeulen model, k_1 is the rate constant of the 1st Vermeulen reaction, k_2 is the rate constant of the 2nd Vermeulen reaction, and f/m express the ratio between the occurred two reactions equals a/1-a. The results are expressed that two models of reactions were happened enclosed a 1st order Vermeulen film reaction and 2nd order Vermeulen as film reaction while mixture equals 1-a (Fig. S6). The first reaction of La express an approximately 1/5 of the whole reaction contribution whereas in the case of Y as 1/7, which mean that the 2nd order reaction was achieved faster than the first one for both La and Y. As for the competitiveness of the elements during the chemical reaction, by plotting the relation between time and the fraction tends to unity~0.9999, it was observed that the Y element exhibited more competition than La according to the obtained values of the rate constant of reaction where k_1-Y (0.02101)> k_1-La (0.0143) and k_2-Y (0.01628) >k_2-La (0.0106) (Table 6).

3.5.5. Thermodynamic Analysis

Further information with thermodynamics features emerges, when analyzing adsorption reaction using the generalized Langmuir equation in 3D representation (Fig. 6b). By including the Van't-Hoff connection in the generalized Langmuir form, the Floatotherm model was developed (Eq. 12) and used to compute the thermodynamic parameters and visualize them in 3D representation.

q(pH0,C0,T)=qm(exp(-DH*1000/(8.314*T)+DS/8.314))*pH0^m*C0^n/(1+(exp(-DH*1000/(8.314*T)+DS/8.314))*pH0^f*C0^e)^g* (12)

Table 6 demonstrated the calculated adsorption capacity and the most important parameters of thermodynamics, with different initial pHs (pH_0) and different initial concentrations (C_0) (mmol.g^{-1}) at different temperatures (T: Kelvin). The positive sign of ΔH refers to an endothermic reaction and its magnitude was about 5.97 and 5.68 kJ.mol^{-1} for La^{3+} and Y^{3+}, respectively. Likewise, the negative sign of ΔG values (in kJ.mol^{-1}) is related to a spontaneous reaction and its magnitude for La^{3+} (16.2-18.3) > Y^{3+} (14.6-16.5) describes the more favorability for La^{3+} ions. On the other hand, ΔS (74.08 and 67.73 kJ.mol^{-1}.K^{-1} for La^{3+} and Y^{3+}, respectively) is an important parameter to demonstrate by the fact that raise in entropy taken place due to exchange of metal ions causing more mobility of ions in the adsorption

process. All these data are in agree with the experimental data.

In Table S2, the mathematical approach's accuracy and dependability for adsorption efficiency for La^{3+} and Y^{3+} is shown. The maximum deviation was ±5.0 %, except for Y^{3+} only one point (pH_0: 3.06, C_0: 0.84 $mmol.L^{-1}$, and temperature 302K) was overestimated by 9%.

On the other hand, according to the obtained data from simulation process, the creation of an automatic control system must be evaluating the correlation factor, which has the uptake values as close as possible to the reality. In this work, by drawing the relation between the measured uptake experimentally against the simulating uptake by utilizing the Gauss model to obtain the lowest possible value of error percentage. the correlation of La^{3+} and Y^{3+} uptake were calculated as shown in Table 5 by applying general model Gauss2 {f(x) =a1*exp(-((x-b1)/c1).^2) + a2*exp(-((x-b2)/c2).^2)} for La^{3+} and general model Gauss3 {f(x) =a1*exp(-((x-b1)/c1).^2) + a2*exp(-((x-b2)/c2).^2)+a3*exp(-((x-b3)/c3).^2)} for Y^{3+}, Where $q_{e,exp}$ is an experimental uptake, q_{calc1} is the calculated uptake with respect to two variables (pH_0 and C_0), q_{calc2} is the calculated uptake in relation to three variables (pH_0, C_0, and T), and x=qLa_{calc2}.

Polyglycidyl-methacrylate (PGMA) functionalized with polyamine and further with phosphonic acid (F-PGMA) was synthesized and thoroughly characterized. The characteristics of this synthesized adsorbent were as follows: particle size 52.92 ±6.6 µm, specific surface area (S_{BET}: 50.54 $m^2.g^{-1}$), average pore diameter 2.52 nm and pore volume of 0.0438 cm^3 STP.g^{-1}.

The maximal adsorption capacity for Y^{3+} and La^{3+} was 0.74 and 0.79 $mmol.g^{-1}$, respectively at optimal pH_0 ~5.0. The equilibrium is achieved after 180/240 min of contact and matches the pseudo-second order (PSO) equation well. The Langmuir model efficiently fits the adsorption isotherms and the REs^{3+} (Y^{3+}/La^{3+}) adsorption process is endothermic, spontaneous, and followed by increasing the randomness in the system. Y^{3+}/La^{3+} desorption is exceedingly efficient using HNO_3 (0.5 M) and could be recycled at least six times. F-PGMA displays outstanding functionality, durability, performance, strength, and stability. Furthermore, a mathematical simulation (using MATLAB codes) is being developed and built based upon the experimental data. The mathematical formulae were validated and confirmed with measured values and the output findings.

4. Conclusion

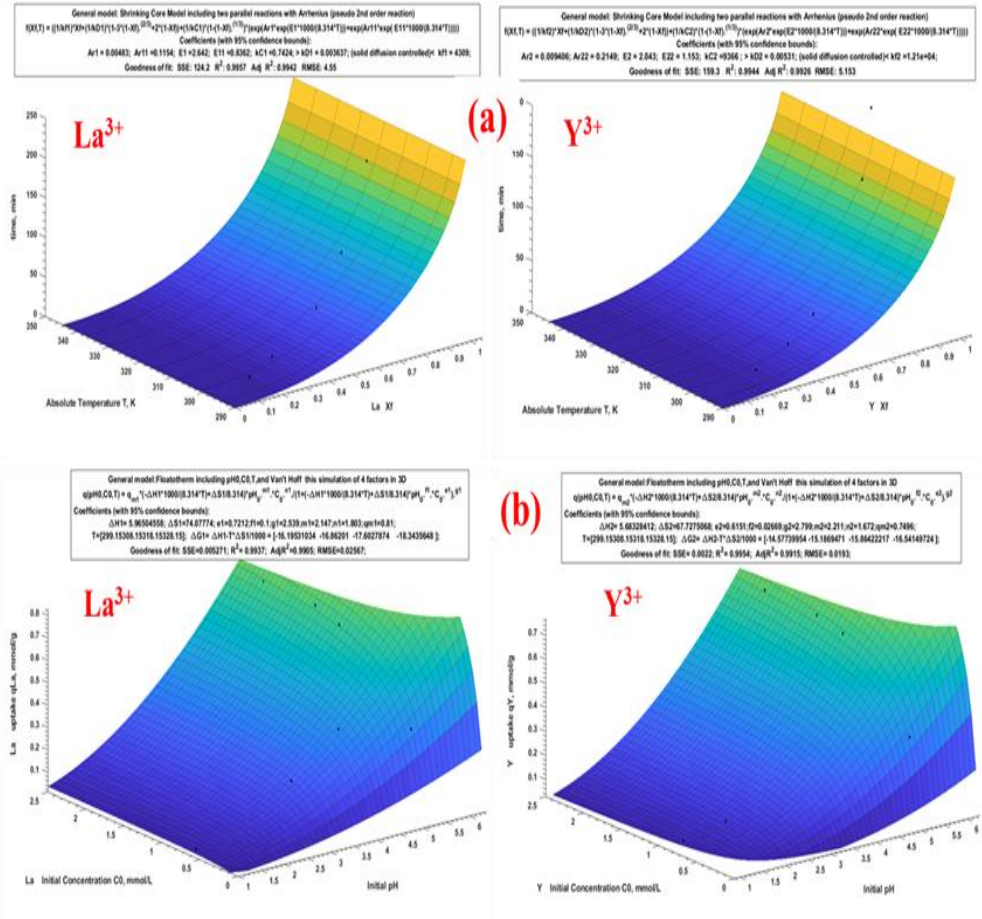

Fig. 6. Shrinking Core Model (a) and Floatotherm model including initial pH_0, C_0, and T with Van't Hoff simulation (b).

Table 6. Different probabilities of variables of Generalized Langmuir model, Pseudo 2nd order model, Shrinking core Model, Modified Vermeulen Model, Floatotherm model (Parameters, constants and goodness of fit).

a) Generalized Langmuir including pH_0 and C_0			**b) Pseudo 2nd order model including Arrhenius Eq.**			**c) Shrinking core model**			**d) Modified Vermeulen Model**			**e) Floatotherm model**		
parameters	La^{3+}	Y^{3+}	parameters	La^{3+}	Y^{3+}	parameters	La^{3+}	Y^{3+}	parameters	La^{3+}	Y^{3+}	parameters	La^{3+}	Y^{3+}
e	1.133	0.940	Ar1	0.005	0.009	Ar1	0.005	0.0094	a	0.189	0.1300	m	11.840	2.211
f	0.042	0.008	Ar2	0.115	0.215	Ar2	0.115	0.2149	k1	0.014	0.0210	n	0.954	1.672
g	1.331	1.332	ΔE1**	2.642	2.043	ΔE1**	2.642	2.043	k2	0.0100	0.0162	e	0.533	0.615
m	2.140	1.948	ΔE2**	0.836	1.153	ΔE2**	0.836	1.153	1-a	0.810	0.869	f	12.240	0.027
n	1.658	1.470	a	1.796	0.579	kC	0.7424	9366	f/m	01:04.	01:06.	g	0.961	2.799
q_m***	0.790	0.740	q_m***	0.791	0.742	kD*	0.0036	0.0053	R^2	0.997	0.99	q_m***	0.810	0.750
ΔG**	-28.465	-25.738	SSE	0.002	0.0007	kf	4309	12100				ΔH**	5.965	5.683
SSE	0.004	0.002	R^2	0.998	0.999	q_m***	0.791	0.7417				ΔS, KJ/mol.K	74.078	67.728
R^2	0.994	0.996	AdjR^2	0.997	0.999	SSE	124.20	159.3				ΔG**, 299	-16.19	-14.57
AdjR^2	0.981	0.990	RMSE	0.015	0.008	R^2	0.996	0.994				ΔG**, 308	-16.86	-15.18
RMSE	0.004	0.028				AdjR^2	0.994	0.993				ΔG**, 318	-17.60	-15.86
						RMSE	4.550	5.153				ΔG**, 328	-18.34	-16.54
												SSE	0.005	0.0022
												R^2	0.994	0.995
												AdjR^2	0.991	0.992
												RMSE	0.026	0.019

Acknowledgments
This work was supported by Nuclear Materials Authority (Egypt). Special dedication to the memory of prof. Dr. Ahmed Donia.

5. References

[1] Chen, Z.; Li, Z.; Chen, J.; Kallem, P.; Banat, F. and Qiu, H.; Recent advances in selective separation technologies of rare earth elements: a review, Journal of Environmental Chemical Engineering, 10, 1, 107104, **2022**. https://doi.org/10.1016/j.jece.2021.107104.

[2] Voncken, J.H.L.; The Rare Earth Elements: An Introduction. SpringerBriefs in Earth Sciences (BRIEFSEARTH), Springer Cham, Switzerland, **2016**.

[3] Galhoum, A.A.; Akashi, T.; Linnolahti, M.; Hirvi, J.T.; Al-Sehemi, A.G.; Kalam, A. and Guibal. E.; Functionalization of poly(glycidylmethacrylate) with iminodiacetate and imino phosphonate groups for enhanced sorption of neodymium - sorption performance and molecular modeling, Reactive and Functional Polymers, 180, 105389, **2022**.https://doi.org/10.1016/j.reactfunctpolym.2022.105389.

[4] Galhoum, A.A.; Elshehy, E.A.; Tolan, D.A.; El-Nahas, A.M.; Taketsugu, T.; Nishikiori, K.; Akashi, T.; Morshedy, A.S. and Guibal, E.; Synthesis of polyaminophosphonic acid-functionalized poly(glycidyl methacrylate) for the efficient sorption of La(III) and Y(III), Chemical Engineering Journal, 375, 121932, **2019**. https://doi.org/10.1016/j.cej.2019.121932.

[5] Balaram,V.; Rare earth elements: A review of applications, occurrence, exploration, analysis, recycling, and environmental impact, Geoscience Frontiers, 10, 4, (1285-1303) **2019**. https://doi.org/10.1016/j.gsf.2018.12.005.

[6] Omodara, L.; Pitkäaho, S.; Turpeinen, E.M.; Saavalainen, P.; Oravisjärvi, K. and Keiski, R L.; Recycling and substitution of light rare earth elements, cerium, lanthanum, neodymium, and praseodymium from end-of-life applications - A review, Journal of Cleaner Production, 236, 117573,**2019**.https://doi.org/10.1016/j.jclepro.2019.07.048.

[7] Talan, D. and Huang, Q.; A review of environmental aspect of rare earth element extraction processes and solution purification techniques; Minerals Engineering, 179, 107430, **2022.**https://doi.org/10.1016/j.mineng.2022.107430.

[8] Iftekhar, S.; Ramasamy, D.L.; Srivastava,V.; Asif, M.B. and Sillanpää, M.; Understanding the factors affecting the adsorption of Lanthanum using different adsorbents: A critical review, Chemosphere, 204, (413-430) **2018**. https://doi.org/10.1016/j.chemosphere.2018.04.053.

[9] Galhoum, A.A.; Eisa, W.H.; El-Sayed, I.E.T.; Tolba, A.A.; Shalaby, Z.M.; Mohamady, S.I.; Muhammad, S.S.; Hussien, S. S.; Akashi, T. and Guibal, E.; A new route for manufacturing poly(aminophosphonic)-functionalized poly(glycidyl methacrylate)-magnetic nanocomposite - Application to uranium sorption from ore leachate, Environmental Pollution, 264, 114797,**2020**.https://doi.org/10.1016/j.envpol.2020.114797.

[10] Al-Ghamdi, A.A.; Galhoum, A.A.; Alshahrie, A.; Al-Turki, Y.A.; Al-Amri, A.M. and Wageh, S.; Mesoporous magnetic cysteine functionalized chitosan nanocomposite for selective uranyl ions sorption: experimental, structural characterization, and mechanistic studies, Polymers, 14, 13, 2568, **2022**. https://doi.org/ 10.3390/polym14132568.

[11] Sun, X.; Yang, L.; Xing, H.; Zhao, J.; Li, X.; Huang, Y. and Liu, H.; Synthesis of polyethylenimine-functionalized poly(glycidyl methacrylate) magnetic microspheres and their excellent Cr(VI) ion removal properties,

Chemical Engineering Journal, 234, (338-345) **2013**. https://doi.org/10.1016/j.cej.2013.08.082.

[12] Al-Ghamdi, A.A.; Galhoum, A.A.; Alshahrie, A.; Al-Turki, Y.A.; Al-Amri, A.M. and Wageh, S.; Mechanistic studies of uranyl interaction with functionalized mesoporous chitosan-superparamagnetic nanocomposites for selective sorption: Characterization and sorption performance. Mater. Today Commun., 33, 104536, **2022**. https://doi.org/10.1016/j.mtcomm.2022.104536.

[13] Davidescu, C.-M., Ciopec, M.; Negrea, A.; Popa, A.; Lupa, L.; Dragan, E.-S.; Ardelean, R.; Ilia, G. and Iliescu, S.; Synthesis, characterization, and Ni(II) ion sorption properties of poly(styrene-co-divinylbenzene) functionalized with aminophosphonic acid groups, Polymer Bulletin, 70, (277-291) **2013**. https://doi.org/10.1007/s00289-012-0801-3.

[14] El-Boraey, H.A.L.; El-Gokha, A.A.A.; El-Sayed, I.E.T. and Azzam, M.A.; Transition metal complexes of α-aminophosphonates Part I: synthesis, spectroscopic characterization, and in vitro anticancer activity of copper(II) complexes of α-aminophosphonates, Medicinal Chemistry Research, 24, (2142-2153) **2015**. https://doi.org/10.1007/s00044-014-1282-8.

[15] Fouda, S.R.; El-Sayed, I.E.; Attia, N.F.; Abdeen, M.M.; Abdel Aleem, A.A. H.; Nassar, I.F.; Mira, H.I.; Gawad, E.A.; Kalam, A. and Al-Ghamdi, A.A.; Mechanistic study of Hg(II) interaction with three different α-aminophosphonate adsorbents: Insights from batch experiments and theoretical calculations, Chemosphere, 304, 135253, **2022**. https://doi.org/10.1016/j.chemosphere.2022.135253.

[16] Boyadjiev, C.; Theoretical Chemical Engineering: Modeling and Simulation. Springer Berlin Heidelberg, **2010**.

[17] Kawady, N.A.; Gawad, E.A.E. and Mubark, A.E. ; Modified grafted nano cellulose based bio-sorbent for uranium (VI) adsorption with kinetics modeling and thermodynamics, Korean Journal of Chemical Engineering, 39, (408-422) **2022**. https://doi.org/10.1007/s11814-021-0886-1.

[18] Williams, R. pKa data (accessed on 4/6/2017); http://www.chem.wisc.edu/areas/reich/pkatable/pKa_compilation-1-Williams.pdf.

[19] Fraga, T.J.M.; de Lima, L.E.M.; de Souza, Z.S.B.; Carvalho, M.N.; Freire, E.M.P.d.L.; Ghislandi, M.G. and da Motta, M.A.; Amino-Fe_3O_4-functionalized graphene oxide as a novel adsorbent of Methylene Blue: kinetics, equilibrium, and recyclability aspects, Environ. Sci. Pollut. Res., 26, (28593–28602) **2019**. https://doi.org/10.1007/s11356-018-3139-z.

[20] Viveros-Ceballos, J.; Ordóñez, M.; Sayago, F. and Cativiela, C.; Stereoselective synthesis of α-amino-C-phosphinic acids and derivatives, Molecules, 21, 9, 1141, **2016**. https://doi.org/10.3390/molecules21091141.

[21] Sahin, M.; Kocak, N.; Arslan,G. and Ucan, H.I.; Synthesis of crosslinked chitosan with epichlorohydrin possessing two novel polymeric ligands and its use in metal removal. J. Inorg. Organomet. Polym. Mater., 21 , (69-80) **2011**. https://doi.org/10.1007/s10904-010-9421-2.

[22] Almeida, S.d.N. and Toma, H.E.; Neodymium(III) and lanthanum(III) separation by magnetic nanohydrometallurgy using DTPA functionalized magnetite nanoparticles, Hydrometallurgy, 161, (22-28) **2016**. https://doi.org/10.1016/j.hydromet.2016.01.009.

[23] Wu, D.; Zhao, J.; Zhang, L.; Wu, Q. and Yang,Y.; Lanthanum adsorption using iron oxide loaded calcium alginate beads, Hydrometallurgy, 101, 1-2, (76-83) **2010**. https://doi.org/10.1016/j.hydromet.2009.12.002.

[24] Lv, L.; Zhang, J.; Yuan, S.; Huang, L.; Tang, S.; Liang, B. and Pehkonen, S.O.; Enhanced adsorption of Cu(II) ions on chitosan microspheres functionalized with polyethylenimine-conjugated poly(glycidyl methacrylate) brushes, RSC Adv., 6, (78136-78150) **2016**. https://doi.org/10.1039/C6RA16226F.

[25] Wang, W.; Zhang, Q.; Zhang, B.; Li, D.; Dong, X.; Zhang, L. and Chang, J.; Preparation of monodisperse, superparamagnetic, luminescent, and multifunctional PGMA microspheres with amino-groups, Chin. Sci. Bull., 53, (1165-1170) **2008**. https://doi.org/10.1007/s11434-007-0512-6.

[26] Tang, Y.; Ma, Q.; Luo, Y.; Zhai, L.; Che, Y. and Meng, F.; Improved synthesis of a branched poly(ethylene imine)-modified cellulose-based adsorbent for removal and recovery of Cu(II) from aqueous solution, J. Appl. Polym. Sci., 129, (1799-1805) **2013**. https://doi.org/10.1002/APP.38878.

[27] Bondar, Y.V.; Kim, H.J. and Lim, Y.J.; Sulfonation of (glycidyl methacrylate) chains grafted onto nonwoven polypropylene, J. Appl. Polym. Sci., 104, (3256-3260) **2007**. https://doi.org/10.1002/app.25887.

[28] Coates, J.; Interpretation of Infrared Spectra, A Practical Approach, in Encyclopedia of Analytical Chemistry, R.A. Meyers, Editor., John Wiley & Sons Ltd: Chichester, U.K. (p. 10815-10837) **2000**.

[29] Zenobi, M.C.; Luengo, C.V.; Avena, M.J. and Rueda, E.H.; An ATR-FTIR study of different phosphonic acids adsorbed onto boehmite,

Spectrochim. Acta, Part A, 75, 4, (1283-1288) **2010**. https://doi.org/10.1016/j.saa.2009.12.059.

[30] Popa, A., Ene, R.; Visinescu, D.; Dragan, E.S.; Ilia, G.; Iliescu, S. and Parvulescu, V.; Transitional metals immobilized by coordination on aminophosphonate functionalized copolymers and their catalytic properties, J. Mol. Catal. A, 408, (262-270) **2015**.https://doi.org/10.1016/j.molcata.2015.07.035.

[31] Caykara, T.; Cakar, F. and Demirci, S. A.; New type of poly(glycidyl methacrylate) microbeads with surface grafted iminodiacetic acid: Synthesis and characterization, Polym. Bull., 61, (311-318) **2008**. https://doi.org/10.1007/s00289-008-0958-y.

[32] Iftekhar, S.; Srivastava, V. and Sillanpaa, M.; Synthesis and application of LDH intercalated cellulose nanocomposite for separation of rare earth elements (REEs), Chem. Eng. J., 309, (130-139) **2017**. https://doi.org/10.1016/j.cej.2016.10.028.

[33] Awad, F.S.; AbouZied, K.M.; Abou El-Maaty, W.M.; El-Wakil, A.M. and El-Shall, M. S.; Effective removal of mercury(II) from aqueous solutions by chemically modified graphene oxide nanosheets, Arabian Journal of Chemistry, 13, 1, (2659-2670) **2020**. https://doi.org/10.1016/j.arabjc.2018.06.018.

[34] Wang, Z.; Yin, P.; Wang, Z.; Qu, R. and X.Liu.; Chelating Resins Silica Gel Supported Aminophosphonic Acids Prepared by a Heterogeneous Synthesis Method and a Homogeneous Synthesis Method and the Removal Properties for Hg(II) from Aqueous Solutions, Industrial & Engineering Chemistry Research, 51, 25, (8598-8607) **2012**. https://doi.org/10.1021/ie3002233.

[35] Morshedy, A.S.; Galhoum, A.A.; Abdel Aleem, A. Aleem H.; Shehab El-din, M.T.; Okaba, D.M.; Mostafa, M.S.; Mira, H.I.; Yang, Z. and El-Sayed, I.E.T.; Functionalized aminophosphonate chitosan-magnetic nanocomposites for Cd(II) removal from aqueous solutions: Performance and mechanisms of sorption, Appl. Surf. Sci., 561, 150069, **2021**. https://doi.org/10.1016/j.apsusc.2021.150069.

[36] Wu, H.; Chi, F.; Zhang, S.; Wen, J.; Xiong, J. and Hu, S.; Control of pore chemistry in metal-organic frameworks for selective uranium extraction from seawater, Microporous and Mesoporous Materials, 288, 109567, **2019**. https://doi.org/10.1016/j.micromeso.2019.109567.

[37] Tien,C.; Adsorption calculations and modeling, Boston: Butterworth-Heinemann, **1994**.

[38] Li, F.; Li, D.; Li, X.; Liao, J.; Li, S.; Yang, J.; Yang, Y.; Tang, J. and Liu, N.; Microorganism-derived carbon microspheres for uranium removal from aqueous solution, Chemical Engineering Journal, 284, (630-639) **2016**. https://doi.org/10.1016/j.cej.2015.09.015.

[39] Kyzas, G.Z.; Travlou, N.A. and Deliyanni, E.A.; The role of chitosan as nanofiller of graphite oxide for the removal of toxic mercury ions, Colloids and Surfaces B: Biointerfaces, 113, (467-476) **2014**. https://doi.org/10.1016/j.colsurfb.2013.07.055.

[40] Hubbe, M.A.; Azizian, S. and Douven, S.; Implications of apparent pseudo-second-order adsorption kinetics onto cellulosic materials: A review, J BioResources, 14, 3, (7582-7626) **2019**.

[41] Pan, S.-Y.; Syu, W.-J.; Chang, T.-K. and Lee, C.-H.; A multiple model approach for evaluating the performance of time-lapse capsules in trapping heavy metals from water bodies, RSC Advances, 10, (16490-16501) **2020**. https://doi.org/10.1039/d0ra03017a.

[42] Doğan, M.; Özdemir, Y.; and Alkan, M.; Adsorption kinetics and mechanism of cationic methyl violet and methylene blue dyes onto sepiolite, Dyes and Pigments, 75, 3, (701-713) **2007**.https://doi.org/10.1016/j.dyepig.2006.07.023.

[43] Lima, E.C.; Hosseini-Bandegharaei, A.; Moreno-Piraján, J.C. and Anastopoulos, I.; A critical review of the estimation of the thermodynamic parameters on adsorption equilibria. Wrong use of equilibrium constant in the Van't Hoof equation for calculation of thermodynamic parameters of adsorption, J. Mol. Liq., 273, (425-434) **2019**. https://doi.org/10.1016/j.molliq.2018.10.048.

[44] Imam, E.A.; El-Sayed, I.E.T.; Mahfouz, M.G.; Tolba, A.A.; Akashi, T.; Galhoum, A.A. and Guibal, E.; Synthesis of α-aminophosphonate functionalized chitosan sorbents: Effect of methyl vs phenyl group on uranium sorption, Chem. Eng. J., 352, (1022-1034) **2018**. https://doi.org/10.1016/j.cej.2018.06.003.

[45] Atia, A.A.; Donia, A.M. and Al-Amrani, W.A.; Effect of amine type modifier on the uptake behaviour of silica towards mercury(II) in aqueous solution, Desalination, 246, 1-3, (257-274) **2009**. https://doi.org/10.1016/j.desal.2008.03.055.

[46] Lu, J.; Wu, X.; Li, Y.; Cui, W. and Liang, Y.; Modified silica gel surface with chelating ligand for effective mercury ions adsorption, Surfaces and Interfaces, 12, (108-115) **2018**. https://doi.org/10.1016/j.surfin.2018.04.005.

[47] Alghamdi, N.A.; Mesoporous magnetic-polyaminated-chitosan nanocomposite for selective uranium removal: performance and mechanistic studies, Int. J. Environ. Sci.

Technol. , **2022**. https://doi.org/10.1007/s13762-022-04565-2.

[48] Wu, J.; Ahn, J. and Lee, J.; Kinetic and Mechanism Studies Using Shrinking Core Model for Copper Leaching from Chalcopyrite in Methanesulfonic Acid with Hydrogen Peroxide, Mineral Processing and Extractive Metallurgy Review, 42, 1, (38-45) **2021**. https://doi.org/10.1080/08827508.2020.1795850.

[49] Van Assche, T.R.C.; Baron, G.V. and Denayer, J.F.M.; An explicit multicomponent adsorption isotherm model: accounting for the size-effect for components with Langmuir adsorption behavior, Adsorption, 24, (517-530) **2018**. https://doi.org/10.1007/s10450-018-9962-1.

[50] Jadhav, A.J. and Srivastava,V.C.; Multicomponent adsorption isotherm modeling using thermodynamically inconsistent and consistent models. AIChE Journal, 65, 11, e16727, **2019**. https://doi.org/10.1002/aic.16727.